Supporting Information

Chlorinated-$Ti_3C_2T_F$ as Dual Functional Buried-Interface on SnO_2 Electron Transporting Layer for 25.09% High Performance *n-i-p* Perovskite Solar Cells

Ji Cao,[a, b] Qiaoyun Chen,[a] Wenting Wu,[a] Jianfei Fu,[a, c] Zelong Zhang,[a] Lei Chen,[d] Rui Wang,[a, b] Wei Yu ,[a, b] Lijie Wang,[a] Xiaoting Nie,[a, b] Jing Zhang,[d] Yi Zhou,*[a, b] Bo Song *[a] and Yongfang Li *[a, b, e]

[a.]College of Chemistry, Chemical Engineering and Materials Science, Soochow University, Suzhou 215123, P. R. China
[b.]Laboratory of Advanced Optoelectronic Materials, Suzhou Key Laboratory of Novel Semiconductor-optoelectronics Materials and Devices
[c.]School of Materials Science and Engineering (MSE), NingboTech University, Ningbo, 315211, P. R. China
[d.]School of Material Science & Engineering, National Experimental Demonstration Center for Materials Science and Engineering, Jiangsu Province Cultivation Base for State Key Laboratory of Photovoltaic Science and Technology, Changzhou University, Changzhou 213164 Jiangsu, P. R. China
[e.]Beijing National Laboratory for Molecular Sciences, CAS Key Laboratory of Organic Solids, Institute of Chemistry, Chinese Academy of Sciences, Beijing 100190, P. R. China
*Corresponding author. Email: yizhou@suda.edu.cn, songbo@suda.edu.cn, liyf@iccas.ac.cn.

Methods

Materials

ITO-coated glasses for small-scale device and large-scale device (<15 Ω sq^{-1}) were both bought from Advanced Election Technology Co. SnO_2 colloid precursor (15% in H_2O colloidal dispersion) was purchased from Alfa Aesar. Multilayer MXene was purchased from Jilin 11 Technology Co., Ltd. PbI_2 (99.99%), formamidinium iodide (FAI), methylammonium chloride (MACl), methylammonium bromide (MABr), methylammonium iodide (MAI), Spiro-OMeTAD and bis(trifluormethane)sulfonamide lithium salt (Li-TFSI) were purchased from Xi'an Polymer Light Technology Corp. *N,N*-Dimethylformamide (DMF, anhydrous, 99.8%), dimethyl sulfoxide (DMSO, anhydrous, 99.8%), isopropanol (IPA, anhydrous, 99.8%) and chloroform (CF) were acquired from J&K Technology. Chlorobenzene (CB) and acetonitrile were acquired from Sigma−Aldrich.

Preparation of $Ti_3C_2T_{F,\ Cl}$ chloroform solution

First, dispersed multilayer MXene in an aqueous solution, sonicated the solution at 300 W for 0.5, 1.0, 1.5, 2.0 h below 20 °C, and centrifuged the solution at 6000 rpm for 10 minutes to separate the unflaked MXene to obtain the single-layer MXene nanosheet. Then, the MXene nanosheet was reacted with concentrated HCl (9 mol/ml) and stirred for 20, 40, 60 and 80 min at room temperature, to substitute excess terminal groups -OH, -O and -F. Subsequently, washed the treated $Ti_3C_2T_{F,\ Cl}$ nanosheet with deionized water several times until the pH value ≈ 6.5, and dried in a vacuum environment. Finally, the dispersion solution can be obtained by dispersing $Ti_3C_2T_{F,\ Cl}$ powder in chloroform.

Perovskite lift-off process

First, PTAA layer (30 mg/ml, toluene) solution was spin coated at 4000 rpm for 25 s and annealed at 150 °C for 15 min. Then the SnO_2 was spin-coated at 3000 rpm for 30 s and annealed at 150 °C for 30 min. After spin coating the perovskite film, Ag electrode (~200 nm) was deposited to ensure that the perovskite film is not easy to break or fold during the stripping process. The obtained multilayer structure sample was immersed in toluene solvent at room temperature for 90 minutes. After the PTAA layer is dissolved by toluene, the perovskite/Ag film naturally separates from the substrate and floats on toluene, and again cleaned the buried interface of the perovskite with toluene to remove the remaining PTAA.

Device fabrication

The Pero-SCs were fabricated with a configuration of ITO/SnO_2 or T-SnO_2/perovskite/Spiro-OMeTAD/MoO_3/Ag. First, ITO was cleaned with deionized water, acetone, ethanol and isopropyl alcohol with sequential ultrasonication, and each solvent was cleaned for twice. Then, treated the ITO with ultraviolet ozone for 15 min. Prepared the SnO_2 nanoparticles solution with the ratio SnO_2: H_2O (1:5, v/v), and sonicated for 30 min. Then spin-coated the SnO_2 nanoparticle at 3000 rpm for 30 s and annealed at 150 °C for 30 min. For T-SnO_2, $Ti_3C_2T_{F,\ Cl}$ dissolved in chloroform was spin-coated onto the SnO_2 at 4000 rpm for 30 s. Perovskite films were fabricated by a two-step deposition. First, dissolved PbI_2 (1.5 mol/L) in DMF/DMSO (9:1, v/v) and stirred on a 70 °C heat plate for 10 h. Under a N_2 atmosphere, spin-coated the PbI_2 solution onto the SnO_2 films at 2000 rpm for 20 s and then annealed at 65 °C for 1 min. Then, a mixture of FAI: MAI: MACl (90 mg: 6.39 mg: 9 mg) dissolved in 1 mL IPA was dripped onto the PbI_2 films for 30 s, annealed the film at 150 °C for 15 min. Subsequently, the hole-transport material Spiro-OMeTAD was deposited on the upper perovskite layer at 3500 rpm for 30 s. Note that Spiro-OMeTAD was dissolved in 1 mL

chlorobenzene (72.3 mg) mixed with 17.5 mL Li-TFSI (520 mg mL^{-1} in acetonitrile) and 28.8 mL 4-tert-butyl-pyridine (tBP). Finally, MoO_3 (8 nm) and Ag (100 nm) were evaporated on top of Spiro-OMeTAD.

Characterization

Film Characterization Measurements

KPFM was measured with peakforce mode using PFQNE-Al conducting tips. C-AFM using TUNA mode was carried out with a bias voltage of 0.5 V. UPS measurement was collected using custom-built ultrahigh vacuum apparatus. SEM and EDS images were acquired on Hitachi SU8010 SEM, and the distribution of perovskite grain size was analyzed using a Nano measurer 1.2 software. XRD data were measured on D2 PHASER diffractometer with Cu Kα radiation (Bruker, Germany). The TEM images were collected using JEOL JEM 2100F operated at 200 kV. GIXRD spectra were recorded by xenocs xeuss 2.0 (France). XPS measurement was conducted on a VG Scientific ESCALab 220 XL electron spectrometer with 300 W Al Kα radiation. Fs-TA was measured with broadband capabilities and 120 fs resolution, and an ultrafast systems helios femtosecond transient absorption spectrometer equipped with UV–visible and near-infrared detectors was used to measure the perovskites samples. TRPL spectroscopy and steady-state photoluminescence PL were measured on an FLS1000 (Edinburgh Instrument, UK), the excitation wavelength was 470 nm. PL mapping was measured on a JMAT-S confocal laser scanning microscope (South Port Co., Ltd., Taiwan).

Device Characterization Measurements

The *J*–*V* characteristics of Pero-SCs were measured under a simulated AM 1.5G spectrum. The external quantum efficiencies (EQEs) were measured by an Enli Technology (Taiwan) EQE measurement system. ACIS measurements were all measured in the dark at room temperature with a biased V_{OC} of the cells. The instrument is an IM6 electrochemical workstation (Zahner Zennium, Germany). The TPV and TPC spectra were measured on TPVC-1G (South Port Co., Ltd.).

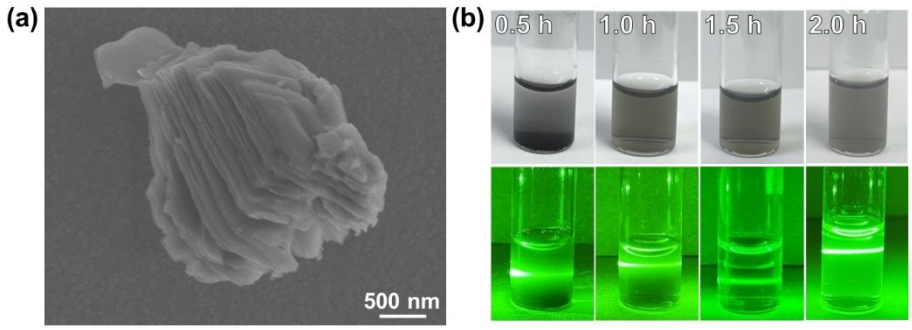

Figure S1. (a) SEM image of commercial MXene; (b) Tyndall phenomenon under different ultrasonic duration.

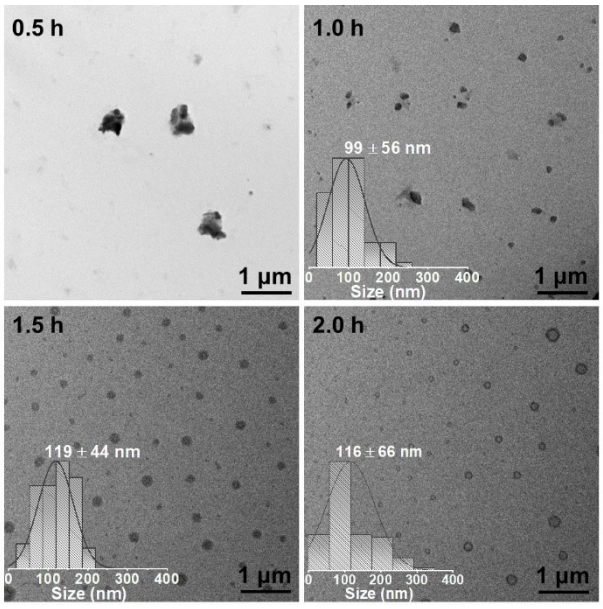

Figure S2. Relationship between ultrasonic time and the size of MXenes through TEM images.

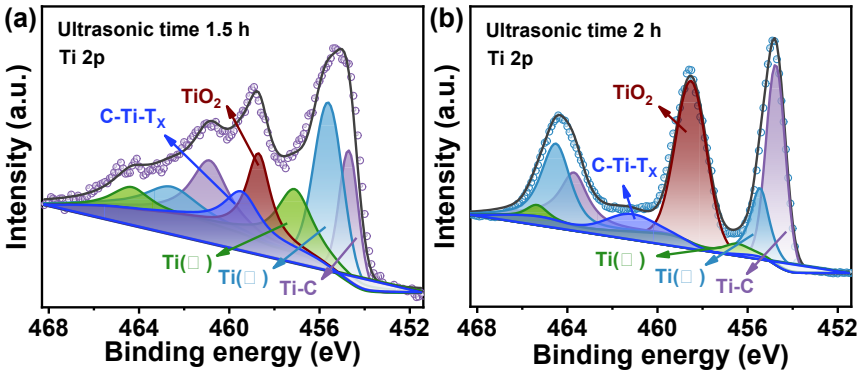

Figure S3. XPS spectra of $Ti_3C_2T_{F,\ Cl}$ after (a) 1.5 hours and (b) 2 hours of ultrasonication.

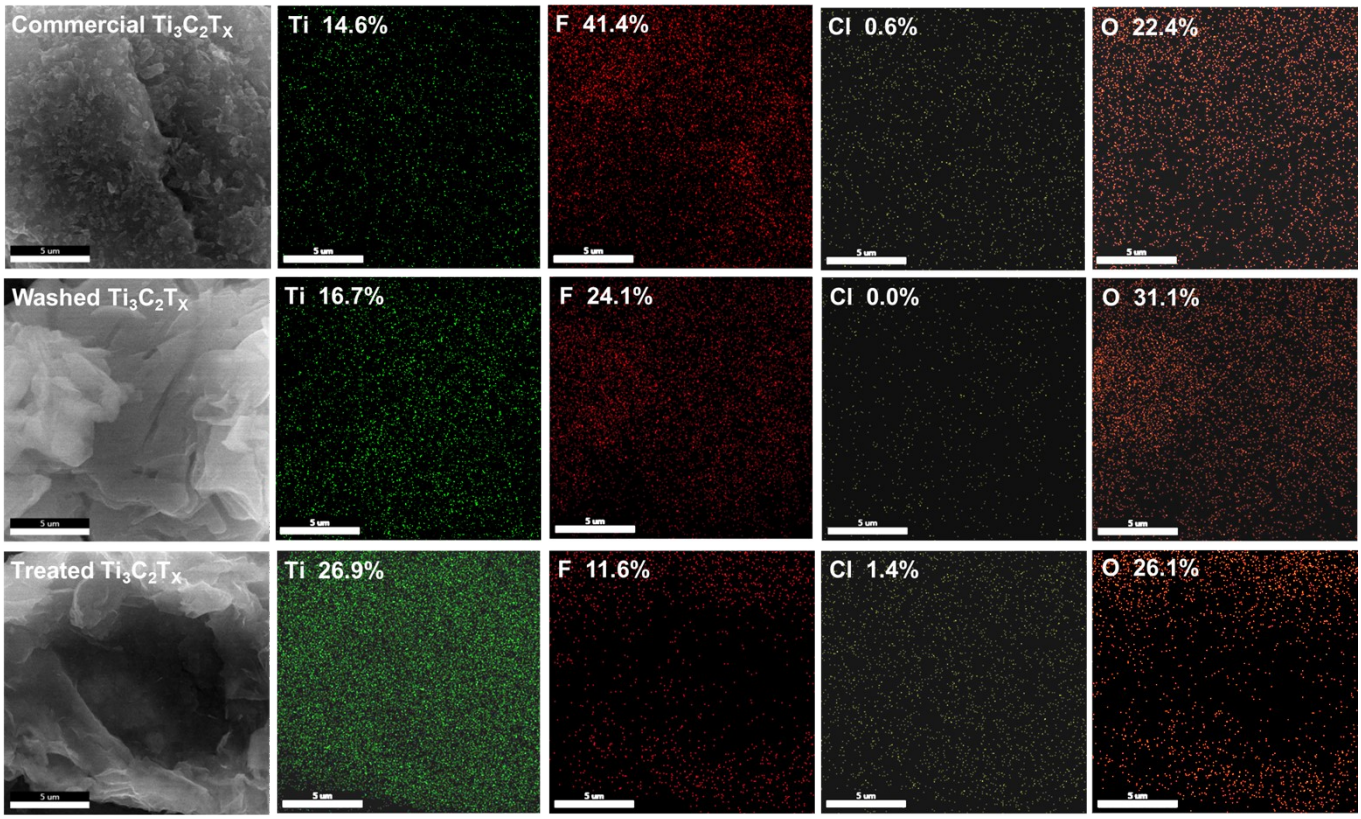

Figure S4. EDS images of (a) commercial Mxene; (b) MXene washed by deionized water; (c) $Ti_3C_2T_{F,\ Cl}$ treated by concentrated hydrochloric acid.

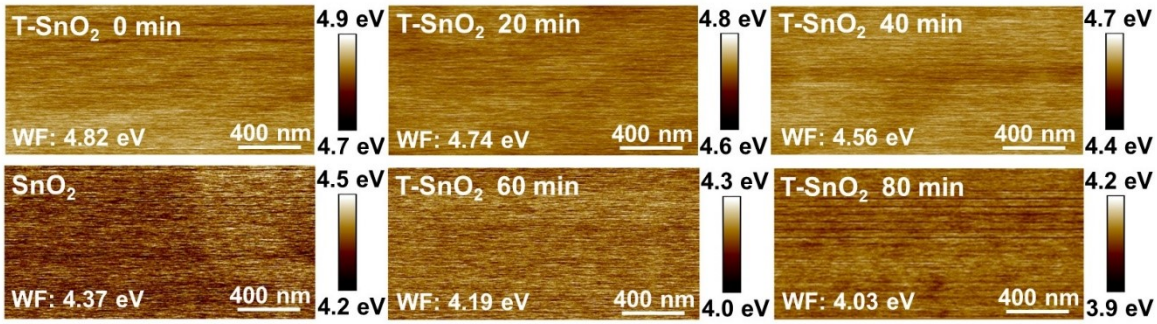

Figure S5. Relationship between acid treatment time and the WF of $Ti_3C_2T_{F,\ Cl}$ through KPFM images.

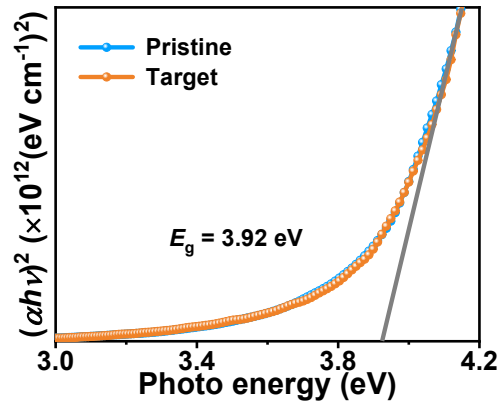

Figure S6. Tauc plots of SnO_2 and T-SnO_2.

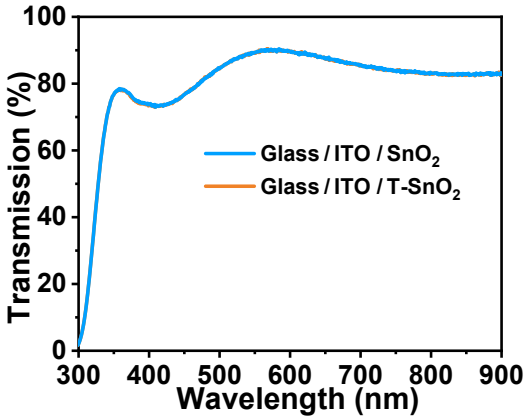

Figure S7. Ultraviolet absorption spectra of SnO_2 and T-SnO_2.

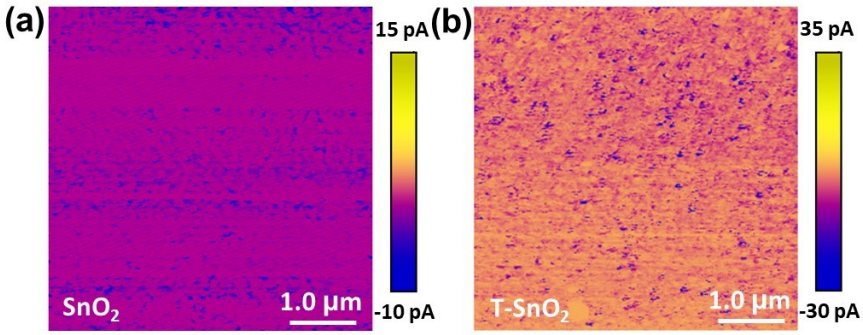

Figure S8. C-AFM images of (a) SnO_2 and (b) T-SnO_2.

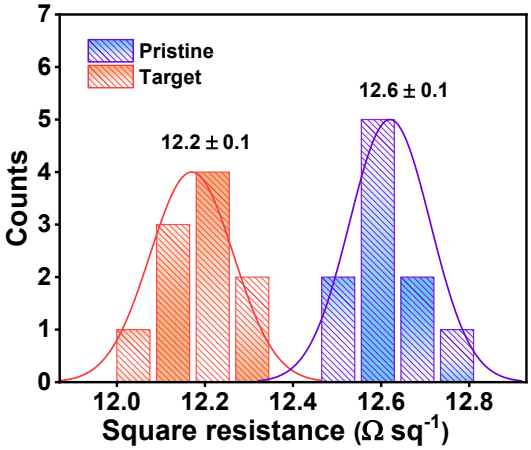

Figure S9. Film surface resistance of ITO/SnO_2 and ITO/T-SnO_2.

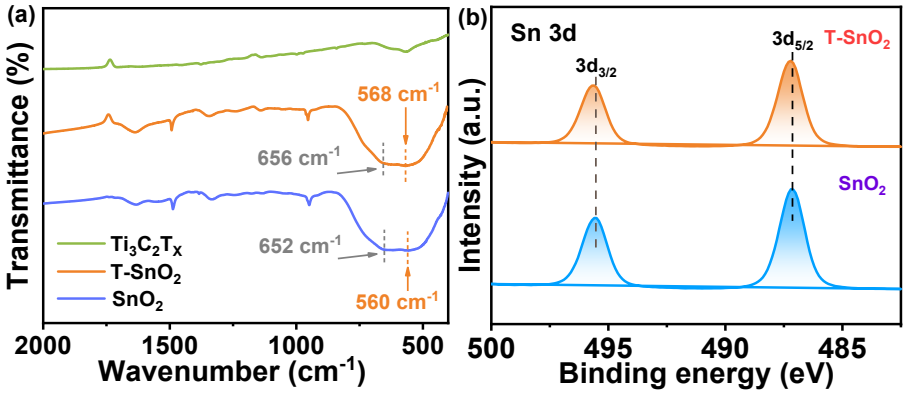

Figure S10. (a) FTIR spectra for SnO_2 and T-SnO_2; (b) XPS spectra of Sn 3d.

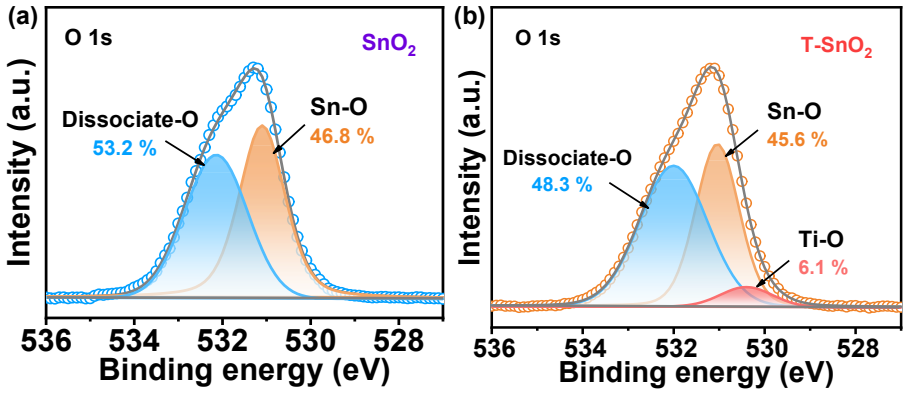

Figure S11. XPS spectra of O 1s of (a) SnO_2 and (b) T-SnO_2.

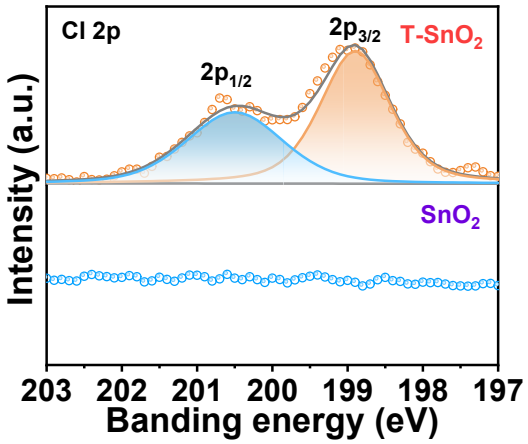

Figure S12. XPS spectra of Cl 1s.

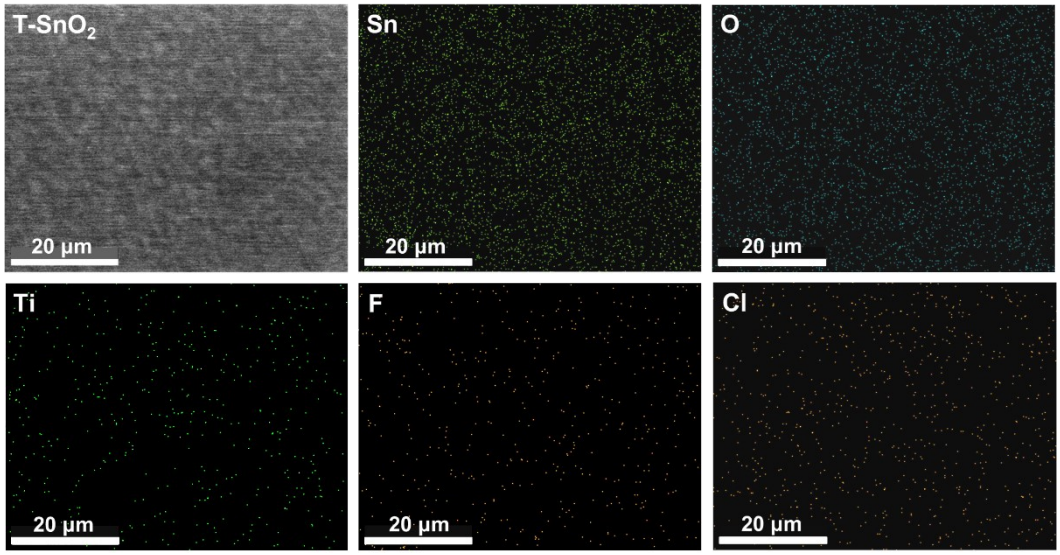

Figure S13. EDS images of T-SnO_2 after flushed by DMF/DMSO (v/v, 9/1).

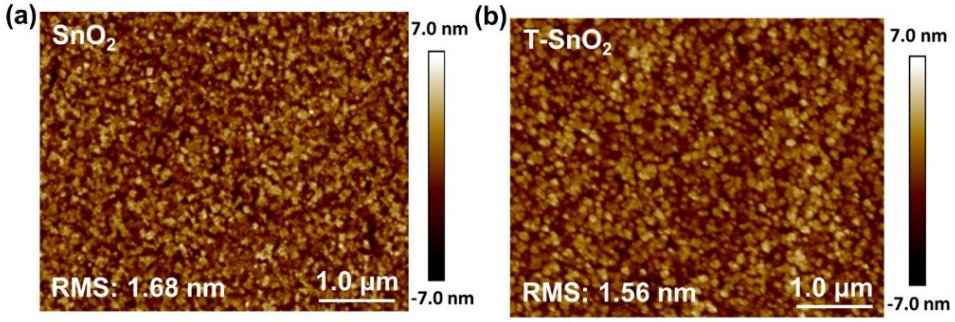

Figure S14. AFM images of (a) SnO_2 and (b) T-SnO_2.

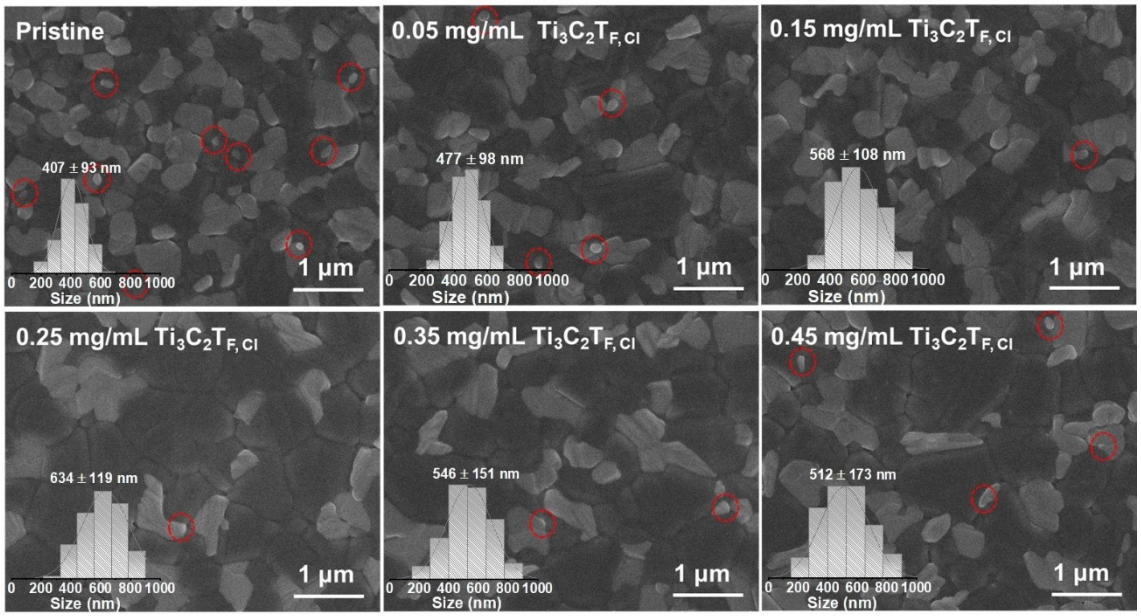

Figure S15. Top-view SEM images of perovskite film after modification with the different concentration of $Ti_3C_2T_{F, Cl}$.

Table S1. The relationship between thickness and concentration of MXene nanosheets.

Concentration (mg/ml)	0.05	0.15	0.25	0.35	0.45

Thickness (nm)	2.6 ± 0.2	3.6 ± 0.2	5.4 ± 0.3	7.5 ± 0.4	9.6 ± 0.3

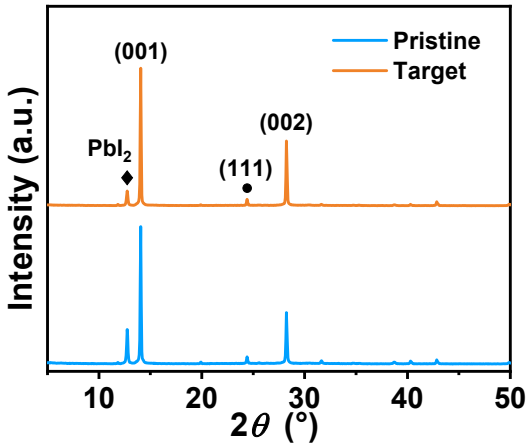

Figure S16. XRD spectra for SnO_2/perovskite and T-SnO_2/perovskite.

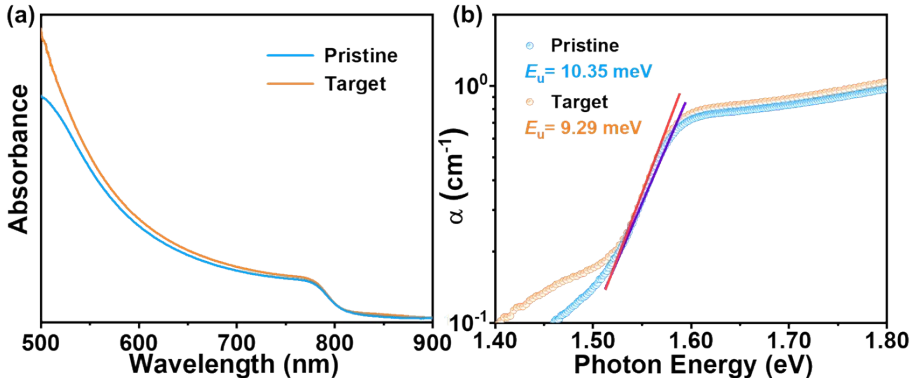

Figure S17. (a) UV–vis absorption spectra and (b) Urbach edge absorption coefficient of SnO_2/perovskite and T-SnO_2/perovskite.

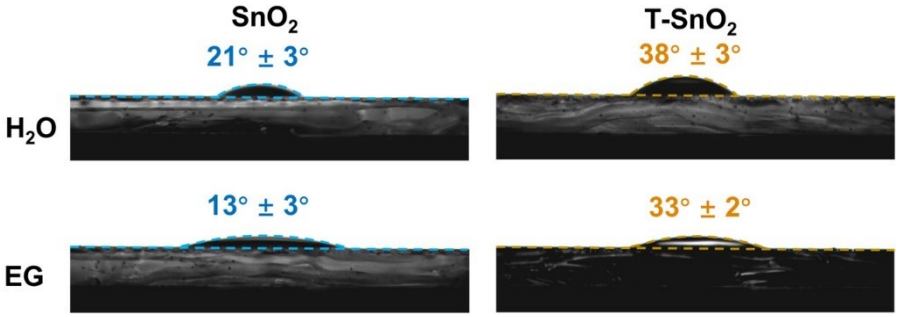

Figure S18. Water and ethylene glycol droplet contact angle measurements on SnO_2 and T-SnO_2.

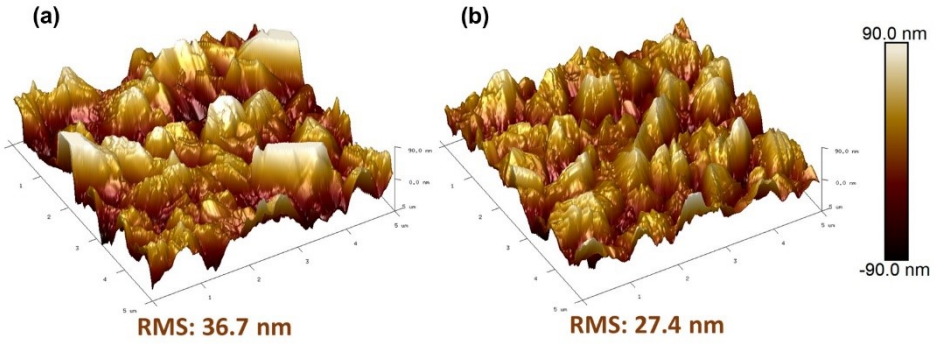

Figure S19. AFM images of (a) perovskite without $Ti_3C_2T_{F,Cl}$ and (b) perovskite with $Ti_3C_2T_{F,Cl}$.

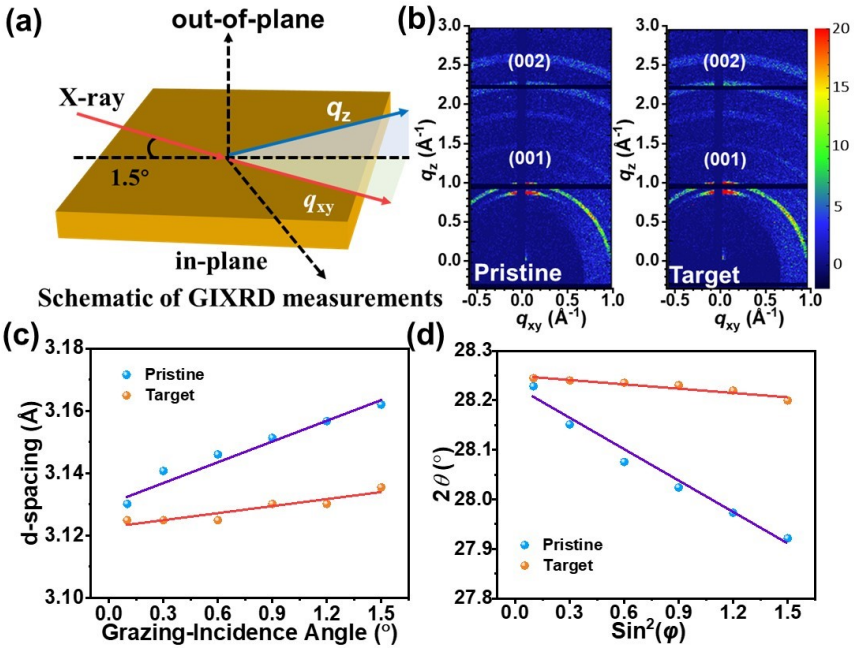

Figure S20. (a) Schematic of 2D GIXRD measurements; (b) 2D GIXRD images; (c) D-spacing values of the (002) plane of the perovskite films depending on the grazing incidence angle; (d) D-spacing values of the (002) plane of the perovskite films depending on the grazing incidence angle.

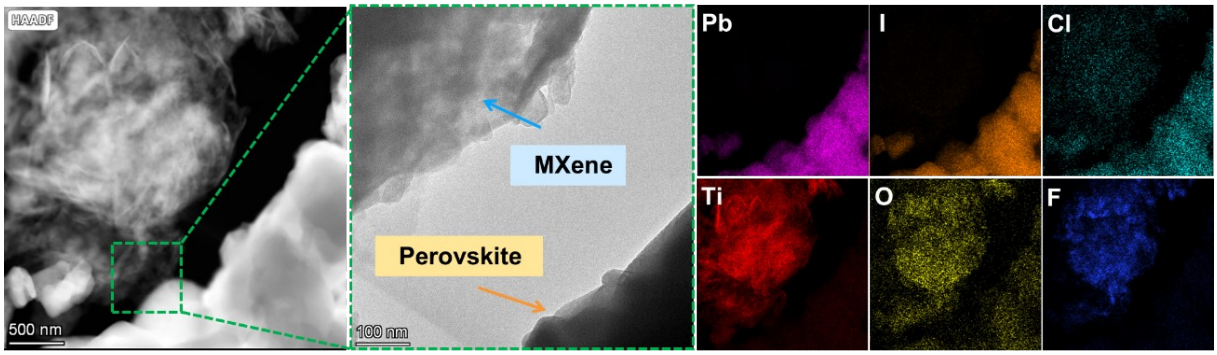

Figure S21. HAADF images of elements distributed on the copper wire mesh.

Note S1. To study whether $Ti_3C_2T_{F,Cl}$ can affect the film quality of the PbI_2 film and subsequently affect the growth of the perovskite, the top-view and cross-sectional morphologies of the PbI_2 films were obtained via SEM (Figure S22). Neither the top-view and sectional SEM images showed observable difference between the pristine and target PbI_2 films. Therefore, it is believed that the difference in the quality of perovskite films is due to the epitaxial growth of perovskite and the change in surface energy.

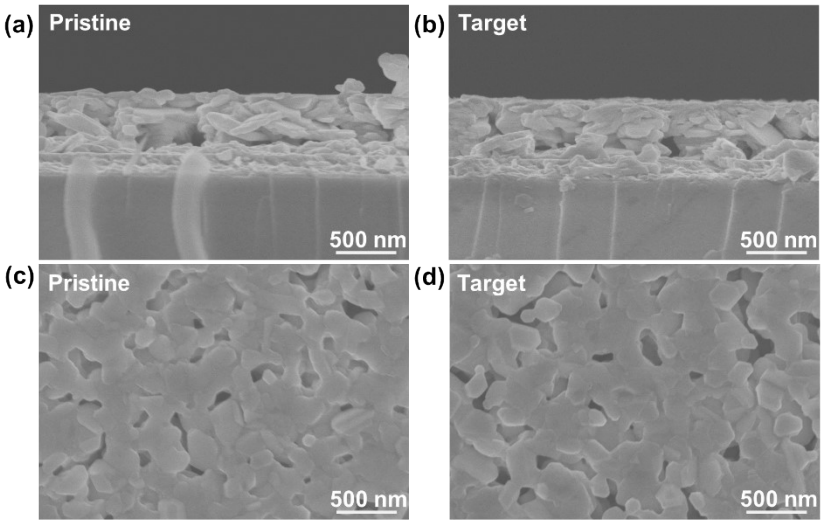

Figure S22. SEM images of the plane and section of the (a-c) pristine PbI_2 and (b-d) target PbI_2.

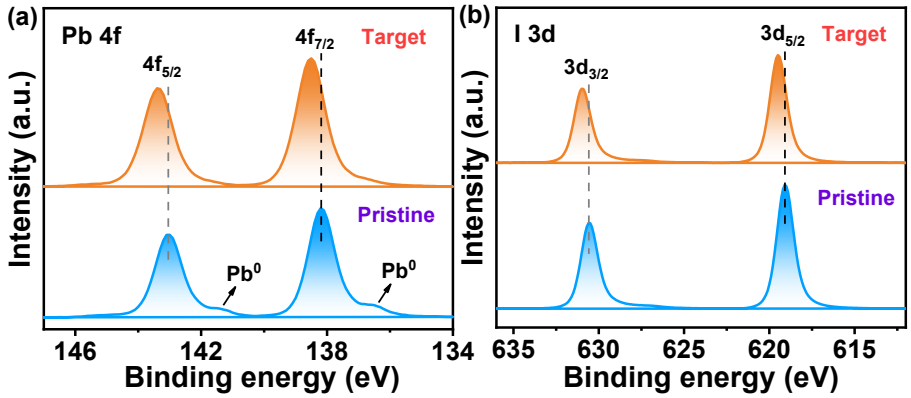

Figure S23. XPS spectra (corrected by the peak of C 1s 284.8 eV) of (a) Pb 4f and (b) I 3d.

Note S2. To further prove the interaction between $Ti_3C_2T_{F,\ Cl}$ and FAI or MAI, Raman spectroscopy was carried out (Figure S23). The BX_6 octahedron shared by the perovskite (ABX_3) is an unstable inorganic cage since the A-site cations (FA, MA) are only loosely bound to the inorganic cage by electrostatic forces. Therefore, A-site cations are able to move freely within the cage void (through translation, rotation and motion), and the vibration of the inorganic cage will show a wider frequency distribution.[1] Figure R17 shows the corresponding spectral region of the perovskite inorganic cage with wavenumbers less than 300 cm^{-1}.[2] The Raman peak of the pristine sample is unevenly widened due to moving A-site cations. In contrast, because the organic cations are locked by $Ti_3C_2T_{F,\ Cl}$ through N-H···F hydrogen bonds and are arranged orderly in the cage void, the Raman peak linewidth is significantly reduced; that is, the dynamic disorder is weakened.[1]

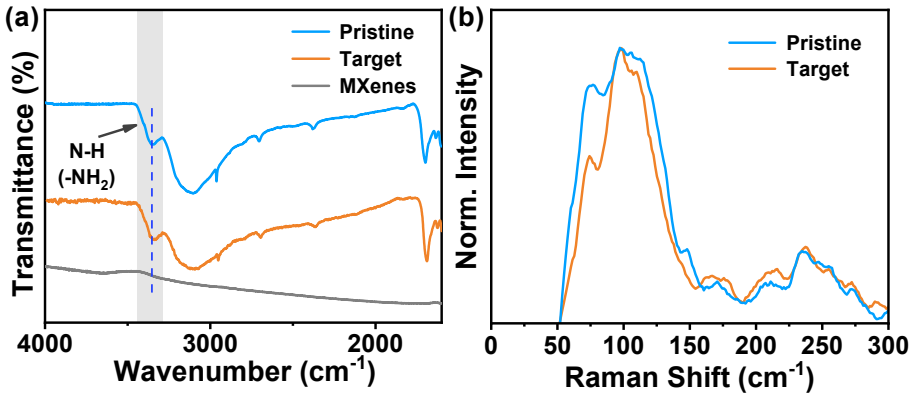

Figure S24. (a) FTIR spectra of SnO_2/perovskite (pristine) and T-SnO_2/perovskite (target); (b) Raman spectra of perovskite in the spectral range of the inorganic cage (the spectra were normalized to their maximum intensity).

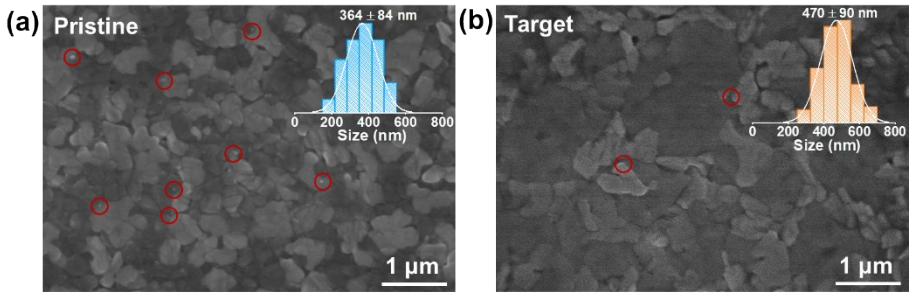

Figure S25. SEM images of the buried interface of the (a) pristine and (b) target perovskite.

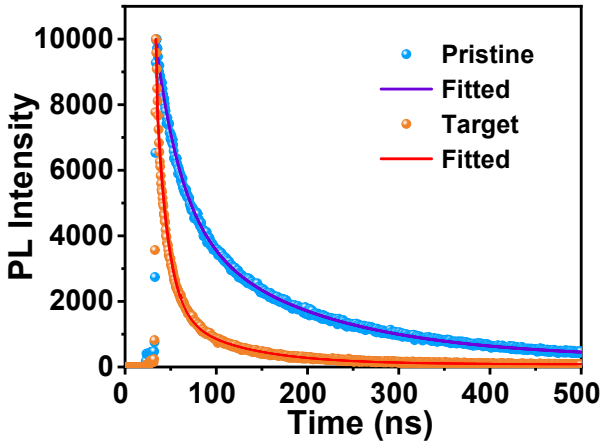

Figure S26. Time-resolved PL spectra.

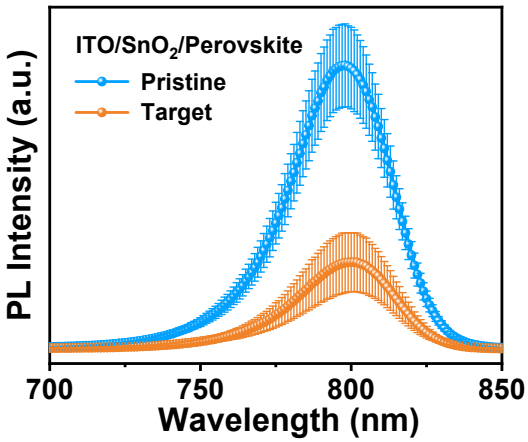

Figure S27. Steady-state PL spectra obtained by multiple curves of structure containing transport layer.

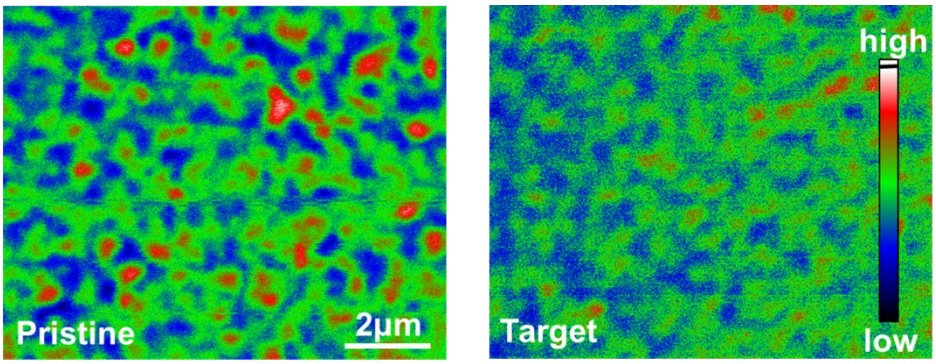

Figure S28. CLSM of the (a) pristine and (b) target.

Table S2. The fitting results of TAS.

Sample	A_1	τ_1 (ps)	A_2	τ_2 (ps)	A_3	τ_3 (ns)
SnO_2/perovskite	-0.960	3.35	-0.029	3770	-0.011	inf
T-SnO_2/perovskite	-0.996	1.37	-0.002	1442	-0.002	inf

Table S3. The fitting results of transient photoluminescence curves.

Sample	f_1 (%)	τ_1 (ns)	f_2 (%)	τ_2 (ns)
SnO_2/perovskite	15.68	2.19	84.32	38.91
T-SnO_2/perovskite	27.72	1.98	72.28	27.63

The TRPL decay can be fitted by a biexponential equation: $I(t) = A_1 e^{(-t/\tau_1)} + A_2 e^{(-t/\tau_2)}$, where τ_1 and τ_2 are the fast and slow decay time components, respectively, and A_1 and A_2 are the relevant decay amplitudes.

Table S4. Photovoltaic parameters derived from pristine Pero-SCs, based on $FA_{0.92}MA_{0.08}PbI_3$.

Number	V_{OC} (V)	J_{SC} (mA cm^{-2})	FF (%)	PCE (%)
1	1.09	24.07	77.55	20.42
2	1.11	23.97	77.00	20.50
3	1.11	24.36	75.82	20.59
4	1.10	23.99	77.83	20.62
5	1.10	24.53	76.67	20.73
6	1.09	24.31	78.58	20.78
7	1.10	24.33	77.67	20.81
8	1.09	24.54	78.13	20.90
9	1.11	24.48	77.04	20.95
10	1.10	24.07	79.18	21.02
11	1.09	24.54	78.60	21.12
12	1.10	24.30	78.89	21.18
13	1.11	24.01	79.46	21.28
14	1.11	24.27	78.87	21.30
15	1.10	24.45	79.18	21.38
16	1.12	24.14	79.17	21.44
17	1.12	24.29	79.01	21.53
18	1.12	24.48	78.39	21.59
19	1.11	24.54	79.51	21.71
20	1.12	24.47	78.91	21.77
21	1.12	24.48	79.66	21.89
22	1.12	24.50	79.71	21.96
23	1.11	25.24	78.48	22.01
24	1.13	25.36	76.37	22.03
25	1.12	25.01	78.99	22.18
26	1.12	25.11	78.86	22.20
27	1.12	25.20	78.83	22.24

28	1.13	24.75	80.02	22.42
29	1.12	25.01	79.9	22.42
30	1.12	25.23	79.24	22.45

Table S5. Photovoltaic parameters derived from target Pero-SCs, based on $FA_{0.92}MA_{0.08}PbI_3$.

Number	V_{OC} (V)	J_{SC} (mA cm^{-2})	FF (%)	PCE (%)
1	1.17	24.47	82.75	23.63
2	1.17	24.56	82.42	23.71
3	1.18	24.88	80.79	23.80
4	1.16	24.58	83.26	23.87
5	1.17	24.84	82.10	23.91
6	1.17	25.37	80.76	23.95
7	1.17	25.02	81.80	24.02
8	1.16	25.22	82.34	24.07
9	1.16	25.25	82.29	24.09
10	1.16	24.74	83.85	24.10
11	1.16	25.32	82.19	24.15
12	1.17	25.22	81.82	24.17
13	1.17	25.12	82.14	24.20
14	1.17	25.11	82.54	24.24
15	1.17	25.26	81.73	24.25
16	1.16	25.18	83.25	24.33
17	1.16	25.10	83.47	24.35
18	1.18	25.47	81.03	24.36
19	1.16	25.10	83.42	24.42
20	1.18	25.39	81.83	24.43
21	1.18	25.37	81.63	24.45
22	1.17	25.38	82.55	24.52
23	1.17	25.00	83.79	24.59
24	1.17	25.47	82.65	24.67
25	1.17	25.91	81.70	24.73
26	1.17	25.35	83.69	24.88
27	1.17	25.50	83.57	24.95
28	1.17	25.71	83.30	25.03
29	1.17	25.95	82.88	25.07
30	1.18	25.81	82.74	25.09

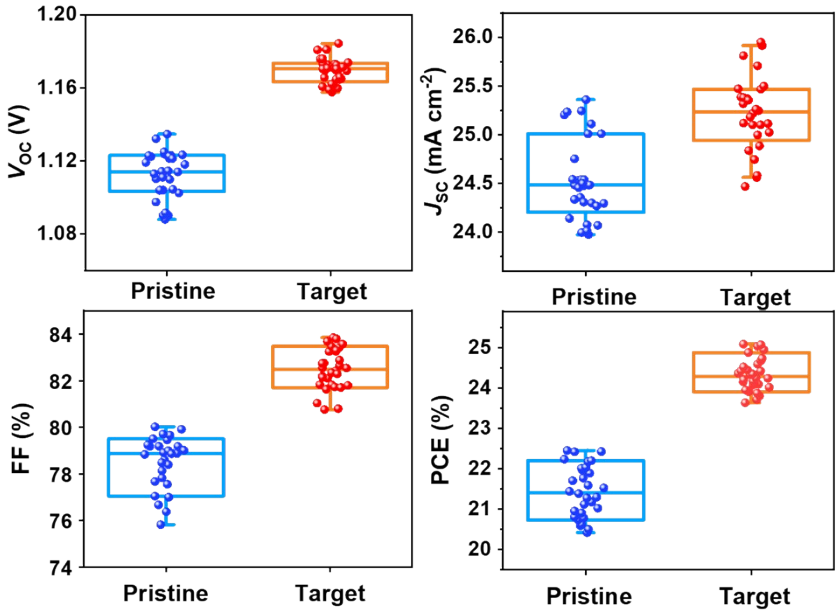

Figure S29. Device performance distribution from 30 cells.

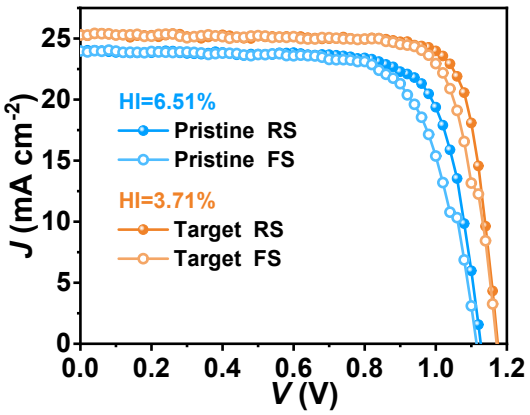

Figure S30. Hysteresis investigation of the Pero-SCs.

Table S6. Hysteresis investigation of the Pero-SCs.

Devices		V_{OC} (V)	J_{SC} (mA cm^{-2})	FF (%)	PCE (%)	h (%)
Pristine	RS	1.13	23.80	76.23	20.43	6.51
	FS	1.11	23.92	71.64	19.10	
Target	RS	1.17	25.33	80.57	23.96	3.71
	FS	1.17	25.22	78.13	23.07	

The semiempirical hysteresis factor (h) is obtained from equation: $h = (PCE_{RS} - PCE_{FS})/PCE_{RS}$, the "FS" is forward scanning and the "RS" is reverse scanning.

Table S7. Parameters fitted from the Nyquist plots for Pero-SCs based on SnO_2 and T-SnO_2.

ETL	R_S (Ω cm^{-2})	R_{tr} (Ω cm^{-2})
SnO_2	26.9	101.4
T-SnO_2	27.7	47.1

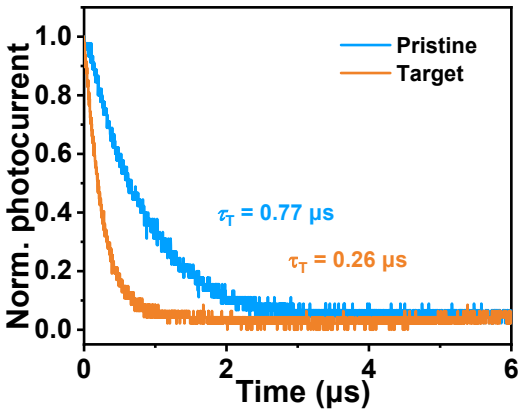

Figure S31. The transient photocurrent measurement in the dark.

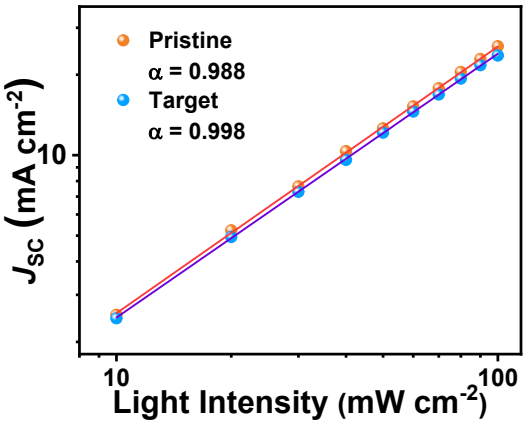

Figure S32. J_{SC} versus light intensity of the Pero-SCs.

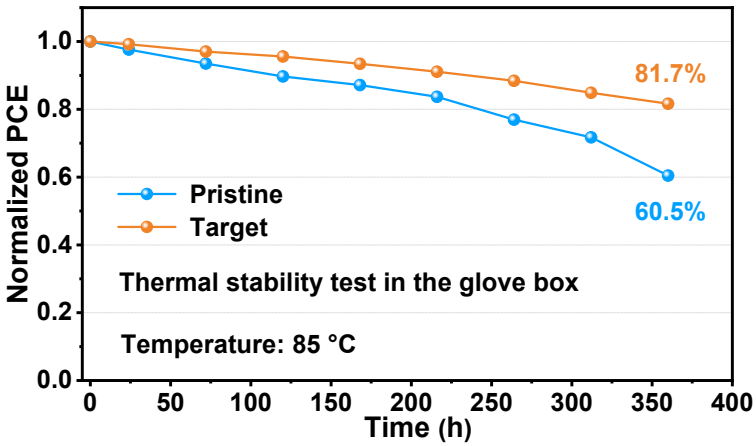

Figure S33. The thermal stability (85 °C) of Pero-SCs in N_2.

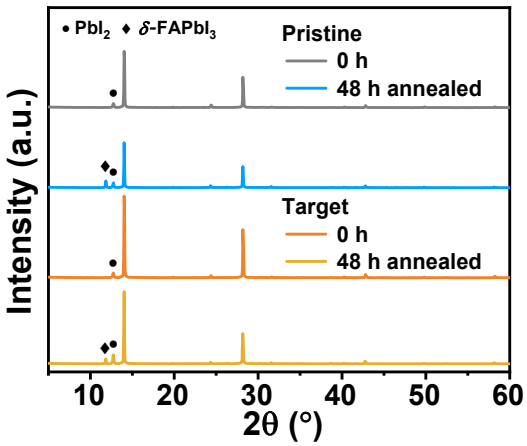

Figure S34. XRD Spectra of the thermal stability (85 °C, in N_2) of perovskite film.

Table S8. The comparison of FF and PCE for the previous studies based on the MXenes modification of *n-i-p* Pero-SCs.

Materials/Methods	Device structure	V_{OC} (V)	J_{SC} (mA cm^{-2})	FF (%)	PCE (%)	Year[Ref]
$Ti_3C_2T_X$/ETL	ITO/SnO_2/$MAPbI_3$/Spiro-OMeTAD/Ag	1.08	22.63	70.0	17.17	2019[3]
HO-$Ti_3C_2T_X$/ETL	ITO/SnO_2/$MAPbI_3$/Spiro-OMeTAD/Ag	1.07	23.11	74.0	18.29	2021[4]
O-$Ti_3C_2T_X$/ETL	FTO/SnO_2/$MAPbI_3$/Spiro-OMeTAD/Ag	1.07	23.88	78.4	20.09	2021[5]
$Ti_3C_2T_X$-SWCNTs/ ETL interface	ITO/SnO_2/FAMAPbIBr/Spiro-OMeTAD/Au	1.07	25.09	80.0	21.42	2021[6]
Nb_2CT_X/ETL additive	ITO/SnO_2/CsFAMAPbIBr/Spiro-OMeTAD/MoO_3/Au	1.14	25.29	79.5	22.86	2021[7]
$Ti_3C_2T_X$MQDs/ ETL additive	ITO/SnO_2/CsFAMAPbIBr/Spiro-OMeTAD/MoO_3/Au	1.17	24.96	79.8	23.34	2021[8]
T-Nb_2CT_X/ETL and perovskite additive	ITO/SnO_2/$FA_{0.85}Cs_{0.15}PbI_3$/Spiro-OMeTAD/Ag	1.12	25.07	77.4	21.79	2022[9]
$Ti_3C_2T_X$-FOTS/ ETL additive	ITO/SnO_2/CsFAMAPbIBr/Spiro-OMeTAD/MoO_3/Ag	1.09	25.22	81.1	22.36	2022[10]
$Ti_3C_2T_X$/ETL additive	ITO/SnO_2/CsFAMAPbIBr/Spiro-OMeTAD/Au	1.13	25.07	81.1	23.07	2022[11]
Nb_2CT_X/Dual interfacial	FTO/SnO_2/CsFAMAPbIBr/Spiro-OMeTAD/Ag	1.25	23.70	79.9	23.68	2022[12]
$Ti_3C_2F_X$/anti-solvent	FTO/TiO_2/$FAPbI_3$/Spiro-OMeTAD/Au	1.13	25.84	82.6	24.17	2022[13]
Nb_2O_5-$Ti_3C_2T_X$/ ET bilayer	FTO/TiO_2/CsFAMAPbIBr/Spiro-OMeTAD/Au	1.07	24.56	73.9	19.46	2023[14]
V_2CT_X/anti-solvent	ITO/SnO_2/CsFAMAPbIBr/Spiro-OMeTAD/Ag	1.18	25.03	79.8	23.47	2023[15]
Au@Nb_2CT_X/ ETL interface	FTO/SnO_2/CsFAMAPbIBr/Spiro-OMeTAD/Au	1.22	24.28	80.6	23.78	2023[16]
$Ti_3C_2T_X$/ETL additive	ITO/TiO_2/$FAPbI_3$/Spiro-OMeTAD/MoO_3/Au	1.18	25.58	81.7	24.63	2023[17]
$Ti_3C_2T_{F,\ Cl}$ / ETL interface	ITO/SnO_2/ $FA_{0.92}MA_{0.08}PbI_3$/Spiro-OMeTAD/MoO_3/Ag	1.18	24.46	83.3	24.05	This work
	ITO/SnO_2/ $FA_{0.85}MA_{0.15}PbI_{2.55}Br_{0.45}$/Spiro-OMeTAD/$MoO_3$/Ag	1.18	25.81	82.7	25.09	

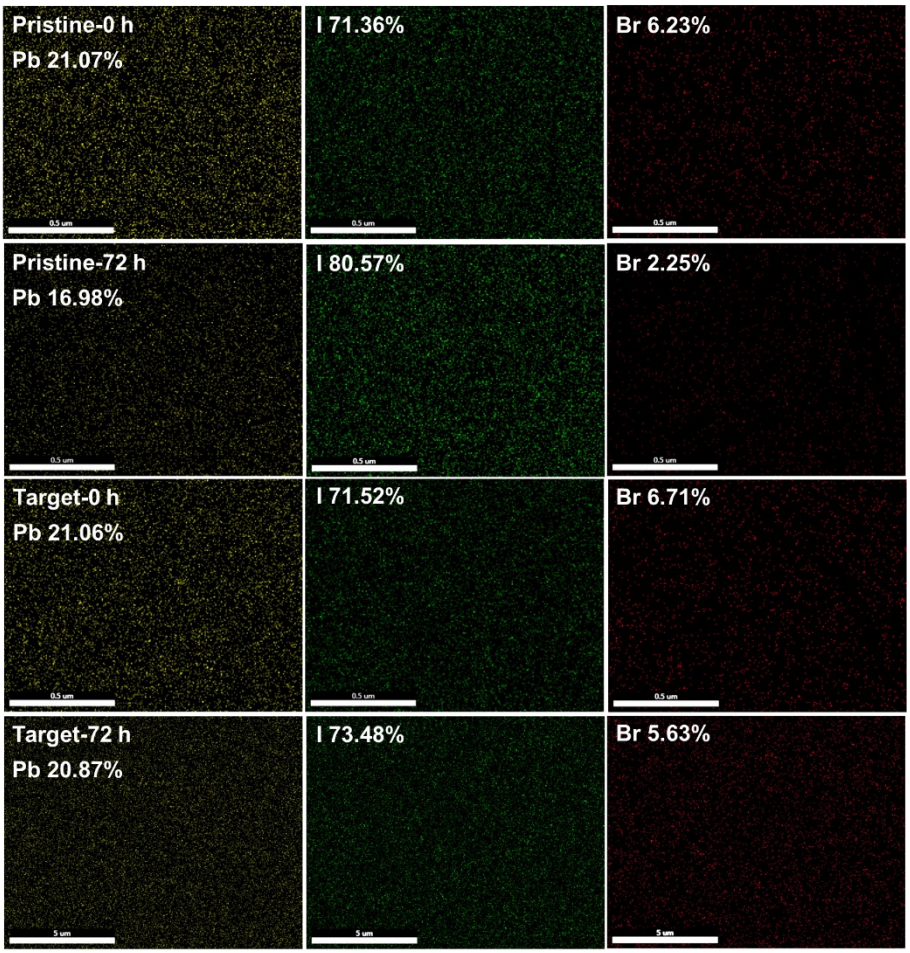

Figure S35. EDS of the mixed halide (I/Br) perovskite before and after heated at 85 °C for 72 h.

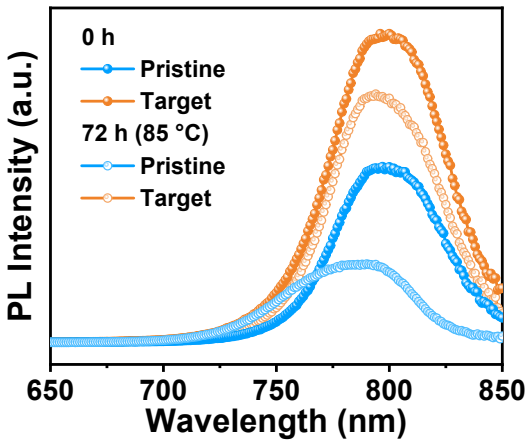

Figure S36. Steady-state PL spectra of the mixed halide (I/Br) perovskite film before and after heated at 85 °C for 72 h.

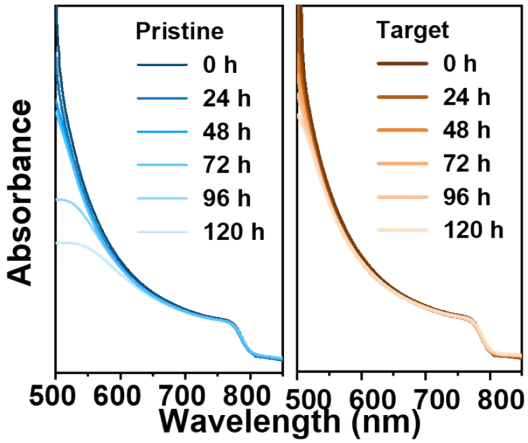

Figure S37. UV-vis spectra of the mixed halide (I/Br) perovskite film before and after heated at 85 °C for 120 h.

Table S9. Photovoltaic parameters of the 1.1 cm^2 devices.

Devices	V_{OC} (V)	J_{SC} (mA cm^{-2})	FF (%)	PCE (%)
Pristine	1.11	25.22	65.45	18.28
Target	1.18	25.48	68.34	20.62

Table S10. Photovoltaic parameters of the Pero-SCs based on $FA_{0.85}MA_{0.15}PbI_{2.55}Br_{0.45}$.

Devices		V_{OC} (V)	J_{SC} (mA cm^{-2})	FF (%)	PCE (%)
Pristine	Best	1.14	24.41	80.56	22.38
	Average	1.12 ± 0.02	23.99 ± 0.41	78.92 ± 0.96	21.43 ± 0.46
Target	Best	1.18	24.46	83.28	24.05
	Average	1.16 ± 0.01	24.17 ± 0.35	83.04 ± 0.89	23.30 ± 0.41

Table S11. Photovoltaic parameters derived from pristine Pero-SCs, based on $FA_{0.85}MA_{0.15}PbI_{2.55}Br_{0.45}$.

Number	V_{OC} (V)	J_{SC} (mA cm^{-2})	FF (%)	PCE (%)
1	1.10	23.61	80.17	20.90
2	1.14	23.32	78.89	20.96
3	1.10	23.91	79.70	20.99
4	1.09	24.48	78.55	21.04
5	1.10	24.05	79.47	21.05
6	1.15	23.23	79.07	21.06
7	1.15	23.45	78.34	21.06
8	1.13	24.21	76.96	21.08
9	1.13	24.46	76.74	21.14
10	1.13	23.80	78.62	21.19
11	1.11	24.17	79.00	21.20
12	1.12	24.09	78.56	21.26
13	1.15	23.34	79.35	21.27
14	1.14	24.24	77.3	21.30
15	1.13	23.49	80.12	21.33
16	1.14	23.83	78.63	21.38

17	1.13	24.19	78.32	21.40
18	1.13	24.29	79.07	21.66
19	1.15	24.03	78.56	21.78
20	1.12	24.30	79.90	21.82
21	1.15	23.69	80.00	21.86
22	1.15	24.56	78.44	22.18
23	1.15	24.29	79.58	22.25
24	1.15	24.46	79.22	22.30
25	1.14	24.41	80.56	22.38

Table S12. Photovoltaic parameters derived from target Pero-SCs, based on $FA_{0.85}MA_{0.15}PbI_{2.55}Br_{0.45}$.

Number	V_{OC} (V)	J_{SC} (mA cm^{-2})	FF (%)	PCE (%)
1	1.14	24.40	81.32	22.65
2	1.15	24.25	81.39	22.72
3	1.15	24.55	80.88	22.77
4	1.16	23.54	83.44	22.84
5	1.17	23.43	83.37	22.89
6	1.16	23.86	82.80	22.92
7	1.15	24.22	82.43	22.97
8	1.17	23.76	82.86	23.02
9	1.16	23.86	83.15	23.06
10	1.14	24.06	84.16	23.10
11	1.14	24.03	84.52	23.15
12	1.16	24.03	83.20	23.19
13	1.16	24.01	83.31	23.20
14	1.16	23.94	84.13	23.29
15	1.17	23.76	83.94	23.33
16	1.16	24.04	83.79	23.41
17	1.16	24.35	83.32	23.48
18	1.15	24.55	83.51	23.55
19	1.16	24.52	83.38	23.64
20	1.18	24.54	82.0	23.72
21	1.16	24.59	83.15	23.77
22	1.17	24.32	83.32	23.79
23	1.17	24.63	82.96	23.92
24	1.19	24.49	82.3	23.95
25	1.18	24.46	83.28	24.05

Table S13. Processing methods of MXenes terminals in Pero-SCs.

Materials	Methods	V_{OC} (V)	J_{SC} (mA cm^{-2})	FF (%)	PCE (%)	Year[Ref]

$Ti_3C_2T_X$ (T=O, F)	UV-ozone treatments $Ti_3C_2T_X$	1.08	22.63	70.0	17.17	2019[3]
$Ti_3C_2Cl_X$	Lewis acidic $CdCl_2$ melts etching	1.70	7.87	82.7	11.08	2021[18]
$Ti_3C_2T_X$ (T=O, F, OH)	$Ti_3C_2T_X$ aqueous solution at 50 °C under stirring in air	1.07	23.11	74.0	18.29	2021[4]
$Ti_3C_2T_X$ (T=O)	$Ti_3C_2T_X$ sintered at 500 °C for 30 min in air	1.07	23.88	78.4	20.09	2021[5]
$Ti_3C_2T_X$-MQDs (T=S, N)	Add $Na_2S_2O_3$ and $NH_3{\cdot}H_2O$ to $Ti_3C_2T_X$ in autoclave at 150 °C for 12 h	1.17	24.96	79.8	23.34	2021[8]
$Ti_3C_2T_X$ (T=AC^-)	Added $Pb(CH_3COO)_2$ to $Ti_3C_2T_X$	1.29	14.96	80.3	15.48	2022[11]
$Ti_3C_2T_X$-MQDs (T=F)	Add Ti_3AlC_2 to HF stir at room temperature for 3 days, and sonicate $Ti_3C_2F_X$ for 30 min at power of 600 W	1.22	20.59	81.6	20.44	2022[19]
$Ti_3C_2T_X$ (T=F/Cl/Br/I)	Add Ti_3AlC_2 to HF acid or molten salts	1.13	25.84	82.6	24.17	2022[13]
$Ti_3C_2Cl_X$	Etch the Al layer in the Ti_3AlC_2 by $ZnCl_2$	1.29	11.56	69.9	10.43	2023[20]
$Ti_3C_2T_{F,\ Cl}$	Add $Ti_3C_2T_X$ to HCl (9 mol/ml) and stirred for 20, 40, 60 and 80 min at room temperature in air	1.18	25.81	82.7	25.09	This work

Notes and references

1 K. Xu, L. Pérez-Fidalgo, B. L. Charles, M. T. Weller, M. I. Alonso and A. R. Goñi, *Scientific Reports*, 2023, **13**, 9300.
2 R. Yan, J. R. Simpson, S. Bertolazzi, J. Brivio, M. Watson, X. Wu, A. Kis, T. Luo, A. R. Hight Walker and H. G. Xing, *ACS Nano*, 2014, **8**, 986–993.
3 L. Yang, C. Dall'Agnese, Y. Dall'Agnese, G. Chen, Y. Gao, Y. Sanehira, A. K. Jena, X. F. Wang, Y. Gogotsi and T. Miyasaka, *Adv. Funct. Mater.*, 2019, **29**, 1905694.
4 L. Yang, D. Kan, C. Dall'Agnese, Y. Dall'Agnese, B. Wang, A. K. Jena, Y. Wei, G. Chen, X.-F. Wang, Y. Gogotsi and T. Miyasaka, *J. Mater. Chem. A*, 2021, **9**, 5016-5025.
5 L. Yang, B. N. Wang, C. Dall'Agnese, Y. Dall'Agnese, G. Chen, A. K. Jena, X. F. Wang and T. Miyasaka, *ACS Sustainable Chem. Eng.*, 2021, **9**, 13672-13680.
6 A. S. R. Bati, M. Hao, T. J. Macdonald, M. Batmunkh, Y. Yamauchi, L. Wang and J. G. Shapter, *Small*, 2021, **17**, e2101925.
7 Y. C. Niu, C. Tian, J. J. Gao, F. Fan, Y. D. Zhang, Y. Y. Mi, X. C. Ouyang, L. N. Li, J. P. Li, S. Y. Chen, Y. P. Liu, H. L. Lu, X. L. Zhao, L. F. Yang, H. X. Ju, Y. G. Yang, C. F. Ding, M. Xu and Q. Xu, *Nano Energy*, 2021, **89**, 106455.
8 Y. Yang, H. Lu, S. Feng, L. Yang, H. Dong, J. Wang, C. Tian, L. Li, H. Lu, J. Jeong, S. M. Zakeeruddin, Y. Liu, M. Grätzel and A. Hagfeldt, *Energy Environ. Sci.*, 2021, **14**, 3447-3454.
9 J. Zhang, C. Huang, Y. Sun and H. Yu, *Adv. Funct. Mater.*, 2022, **32**, 2113367.
10 L. Yin, C. Liu, C. Ding, C. Zhao, I. Z. Mitrovic, E. G. Lim, H. Wang, Y. Sun, Y. Han, Z. Li, L. Yang, C.-Q. Ma and C. Zhao, *Cell Rep. Phys. Sci.*, 2022, **3**, 100905.
11 C. Wu, W. Z. Fang, Q. F. Cheng, J. Wan, R. Wen, Y. Wang, Y. L. Song and M. Z. Li, *Angew. Chem., Int. Ed.*, 2022, **61**, e202210970.
12 Y. Zhang, L. Xu, J. Sun, Y. Wu, Z. Kan, H. Zhang, L. Yang, B. Liu, B. Dong, X. Bai and H. Song, *Adv. Energy Mater.*, 2022, **12**, 2201269.
13 P. F. Guo, C. Liu, X. L. Li, Z. G. Chen, H. F. Zhu, L. G. Zhu, X. H. Zhang, W. H. Zhao, N. Jia, Q. Ye, X. S. Xu, R. H. Chen, Z. Liu, X. L. Fan, C. Y. Zhi and H. Q. Wang, *Adv. Energy Mater.*, 2022, **12**, 2202395.
14 H. G. Lemos, J. H. H. Rossato, R. A. Ramos, J. V. M. Lima, L. J. Affonço, S. Trofimov, J. J. I. Michel, S. L. Fernandes, B. Naydenov and C. F. O. Graeff, *J. Mater. Chem. C*, 2023, **11**, 3571-3580.
15 C. Tian, Y. Yan, S. Feng, J. Wang, Y. Niu, X. Li, H. Ju, Q. Xu, Y. Huang, H. Dong, Z. Liang, B. Dong, L. Li and Y. Yang, *J. Mater. Chem. A*, 2023, **11**, 5015-5026.
16 S. A. Liu, D. L. Zhou, X. M. Zhuang, R. Sun, H. G. Zhang, J. Liang, Y. R. Jia, D. L. Liu and H. W. Song, *ACS Appl. Mater. Interfaces*, 2023, **15**, 3961-3973.
17 Y. Yang, K. Wang, Y. Niu, M. Li, Q. Xu, J. Wang, X.-X. Li, Y. Wang, C.-F. Ding, H. Ju, L. Yang, S. Feng and L. Li, *Sol. RRL*, 2023, **7**, 2300153.
18 Q. Zhou, J. Duan, J. Du, Q. Guo, Q. Zhang, X. Yang, Y. Duan and Q. Tang, *Adv. Sci.*, 2021, **8**, 2101418.
19 D. F. Xu, T. Li, Y. Han, X. X. He, S. M. Yang, Y. H. Che, J. Xu, H. Zou, X. Guo, J. A. Wang, X. R. Lei and Z. K. Liu, *Adv. Funct. Mater.*, 2022, **32**, 2203704.
20 Y. Xu, H. Y. Zhang, Y. Jing, X. Wang, J. Q. Gan, Z. L. Yan, X. Liu, J. H. Wu and Z. Lan, *Appl. Surf. Sci.*, 2023, **619**, 156674.